UNIVERSITY OF CALIFORNIA,
IRVINE

Strain-dependent Optical and Thermal Properties of CNT films

THESIS

Submitted in partial satisfaction of the requirements
for the degree of

MASTER OF SCIENCE

in Mechanical and Aerospace Engineering

by

Hasitha Jeewana Hewakuruppu

Thesis Committee:
Assistant Professor Jaeho Lee, Chair
Professor Yun Wang
Assistant Professor Edwin Peraza Hernandez

2020

Table of Contents

List of Figures

Nomenclature

λ	Wavelength
T	Temperature
d	Diameter of polymer coated CNT fiber
L	Initial length of polymer coated CNT fiber
υ	Poisson's ratio
Ω	Solid angle
ε	Emissivity
A	Area
I_{BB}	Blackbody radiance
h_{ef}	Combined effective heat transmission co-efficient
P_{rad}	Power lost due to thermal radiation
P_{atm}	Power of atmospheric thermal radiation absorbed
P_{sun}	Power of solar radiation absorbed
P_{loss}	Power loss due to convection and conduction

Constants

h	Plank's constant	6.626×10^{-34} J·s
k_b	Boltzmann Constant	1.381×10^{-23} J/K
c	Speed of light	2.998×10^{8}m/s

Acknowledgments

I would like to express my most sincere gratitude to my committee chair, Professor Jaeho Lee, for the invaluable mentorship, guidance and support he has provided me for the past two years. I would like to thank him for suggesting me to pursue this topic and insisting me on finishing my masters with a thesis submission. If not for his continual support and encouragement this thesis would have not been possible

I would also like to thank my committee Members, Professor Yun Wang and Professor Edwin Peraza Hernandez for their meticulous suggestion on making my thesis more scholarly and professional in nature.

In addition, I would like to thank Professor Choongho Yu from Texas A&M University for providing me the CNT film samples and Xia Nie from the NTER lab at University of California Irvine for carrying out the CNT film material characterization.

Finally, and certainly not the least. I would like to thank my beloved parents; I thank them for their unwavering support and unconditional love. I thank them for supporting my educational dreams irrespective of financial burdens and believing in my capability of achieving them. The work presented in this thesis, is my dedication to their love.

Abstract of the Thesis

Strain-dependent Optical and Thermal Properties of CNT films

by

Hasitha Jeewana Hewakuruppu

Master of Science in Mechanical and Aerospace Engineering

University of California, Irvine, 2020

Professor Jaeho Lee, Chair

Passive surface thermal regulation is an area of critical interest, with many potential applications ranging from the design of energy efficient building coatings to applications such as thermo camouflage. The thermoregulation of a surface requires the dynamic modulation of emissivity and reflectivity of the material; these changes are achieved via the manipulation of the surface morphology of the material. The work presented in this thesis used a strain driven CNT film to achieve the said morphology changes. In the experimental characterization of CNT films, a 0.047 increase in the average solar reflectivity was observed when strain up to 80%. When exposed to direct sunlight, this change in reflectivity was manifested as a temperature change of 2.8℃. Following the experimental work, a 3D model was developed to represent the CNT film. The developed model was simulated using raytracing under varying levels of strain, these results were used to develop a hypothesis. The developed hypothesis viewed the surface of the CNT films to be composed of many pit-like structures; the shallowing of the pit depth when strained was determined to be the driving mechanism of increased reflectivity. Later based on the developed hypothesis a simpler periodic model was created to provide an enhanced strain-dependent reflectivity increase of 0.145 in the solar region. This model was further improved by adding a

silver backed layer to provide an increased averaged solar reflectivity of 0.6826 resulting in a surface temperature change of nearly 61℃.

Introduction

All objects above absolute zero are subject to atomic oscillations. These oscillations are physically manifested as the temperature of an object. The chaotic motion of these atoms behaves like accelerating dipoles creating electromagnetic waves [1], these waves are known as thermal radiation. Thermal radiation can be thought of as the conversion of thermal energy of an object to electromagnetic energy. Thus, all objects are constantly losing thermal energy in the form of thermal radiation, this causes the object to gradually loose its temperature; provided that there is no heat input. The relationship between temperature and emitted radiation was quantified by Max Karl Planck in 1896, he states that the radiation spectrum emitted by an object can entirely be determined by the temperature of the object as shown in equation 1 [2].

$$E(\lambda, T) = \frac{2\pi c^2 h}{\lambda^5 (e^{(hc/\lambda k_b T)} - 1)} \qquad \text{Eq. 1}$$

Where E is the radiance, λ the wavelength of radiation, T the absolute temperature, c the speed of light, h the plank constant and k_b the Boltzmann constant. Note the above expression is only valid for an idealized object known as a blackbody which has maximum radiance at all wavelengths. In order to capture the behavior of everyday objects equation 1 needs to be adjusted by multiplying the entire expression by a weighted term know as emissivity (ε). Emissivity is a spectrally varying property $\varepsilon(\lambda)$, i.e. the emissivity value changes with different wavelengths. Emissivity can have any value between zero to one, with one representing a maximum blackbody radiance at that particular wavelength, while zero represents no radiance at all.

It is important to understand that, similar to losing heat due to emanating radiation, an object can also gain heat due to incoming radiation. The efficiency of absorbing incoming radiation is quantified by the spectrally dependent term known as absorptivity. It can be shown by Kirchhoff's law that the emissivity of an object equals its absorptivity [2]. The emissivity/absorptivity of an object can be governed by its intrinsic property as well as due to its unique structure [3].

Due to the spectral nature of emissivity, it plays a critical role in the thermal regulation of an object, this becomes especially apparent in a planetary scale since other forms of heat transfer are not at play. For example, the terrestrial temperature of Earth is maintained by the delicate balance between the incoming solar radiation absorbed by the terrestrial surface and reradiation of excess heat back into space thanks to the atmospheric transparency window.

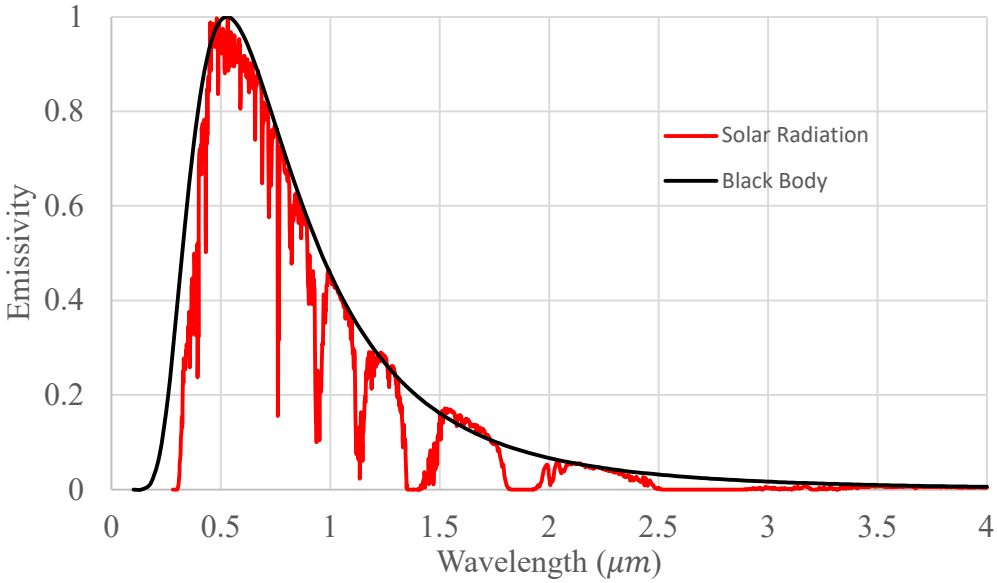

Figure 1: Terrestrial solar radiation on Earth from 0.2 μm till 2.5 μm [4].

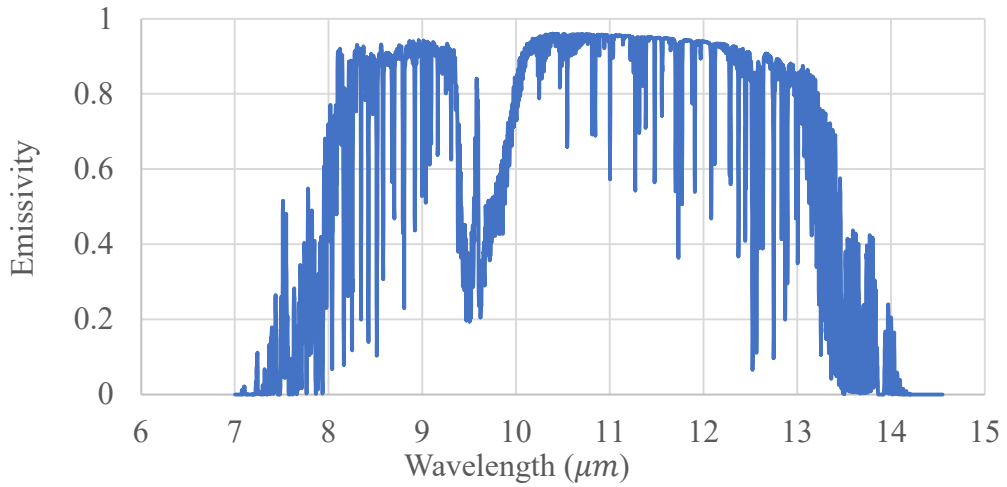

Figure 2: Atmospheric transparency window from 8 μm till 13 μm [5].

The average terrestrial temperature of Earth is around 15℃ which corresponds to a peak radiation of 10 μm, thus it is understood if the absorptivity of Earth was less in the solar region the Earth would be cooler and if its absorptivity was less in the transparency window Earth would be much hotter. Hence, by manipulating the emissivity of surface within the regions of heating and cooling we will be able to precisely manipulate the temperature of a surface. The emissivity profile of an ideal heater and a cooler is shown in figure 3.

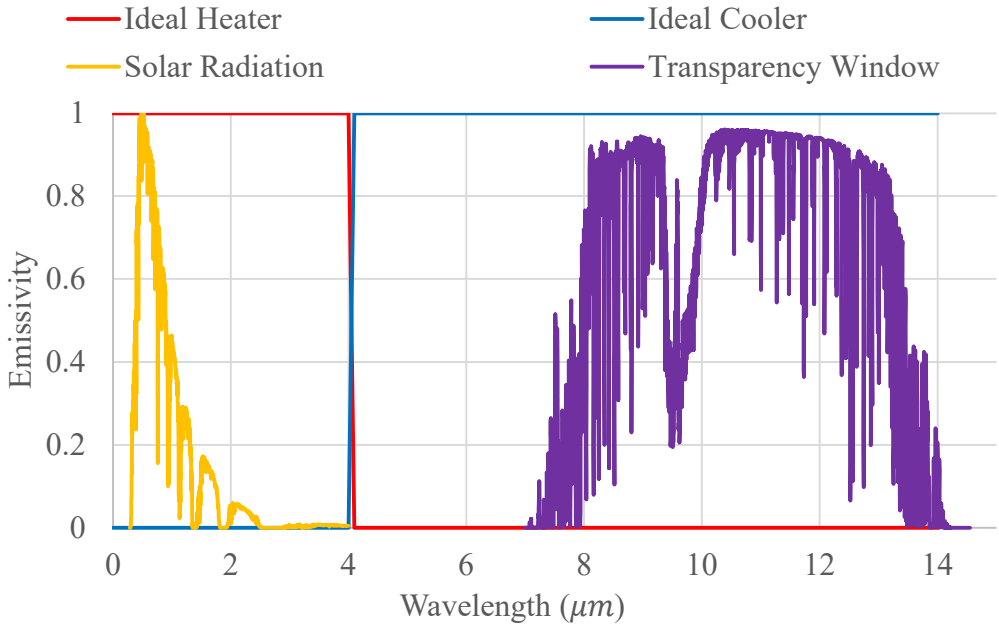

Figure 3: Emissivity profile of an ideal heater and cooler with their corresponding regions of heating and cooling.

Ideal heating is achieved by achieving maximum absorptivity in the solar region and suppressing the emissivity in other regions and ideal cooling is achieved by employing the opposite of this, it is important to note that both these cases of heating and cooling are a completely passive phenomena. Apart from the two extreme cases intermediate levels of both heating and cooling can be used to achieve precise temperature control. The surface emissivity values can also be made dynamic giving the ability to switch between states of cooling and heating allowing for more dynamic temperature control. The associated simulated temperature profiles of an ideal heater and cooler exposed to incident solar radiation for a period of 24 hours are shown in figure 4, (detailed thermal analysis will be discussed in section 3.7).

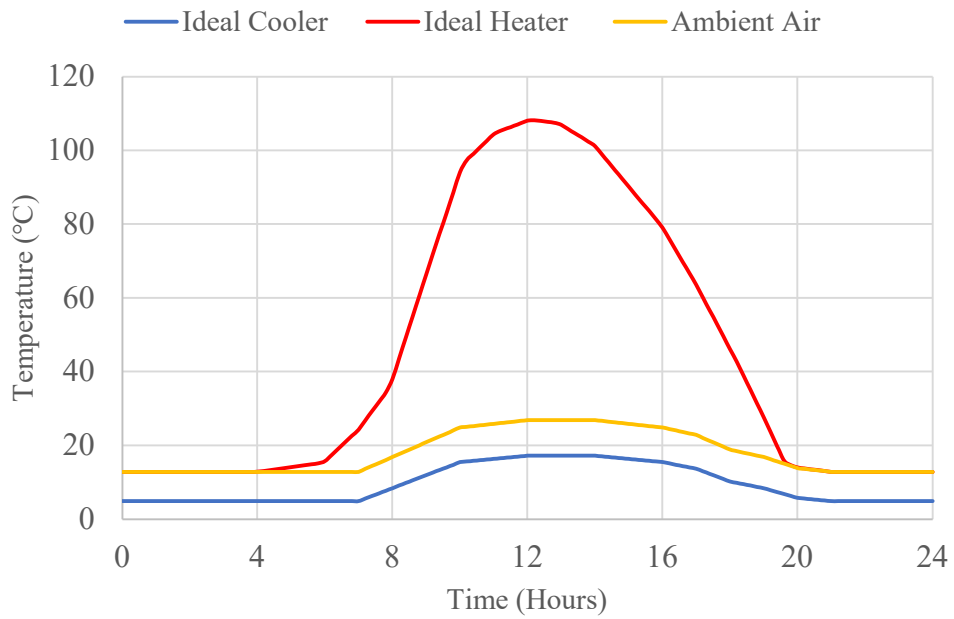

Figure 4: Temporal temperature of profile of an Ideal heater, cooler and ambient air over a period of 24 hours.

During mid-day a significant temperature difference can be observed between the ideal heater and cooler; a temperature difference close to 100℃. This difference in temperature serves as the temperature modulation range.

Thesis Outline

Chapter 1 introduces a brief survey of existing mechanochromic materials; materials that exhibit change in optical properties due to applied mechanical forces. Different mechanism of mechanochromic materials are discussed and their application as thermal switches are evaluated. Chapter 2 focuses on the fabrication procedure of CNT films and their strain-dependent optical properties are presented, later how these properties are manifested as a thermal response when exposed to the Sun is presented. Chapter 3 begins by explaining how the 3D model representing the CNT film is developed and how its change in structural behavior is governed, afterwards the selected method of EM simulation is discussed and how it is implemented is presented to the reader. The simulated results of raytracing are presented and a hypothesis to explain the mechanism behind the strain-dependent reflectivity is developed, this proposed hypothesis is verified by additional simulations. Following the previous work, a justification for the validity of using a geometric approach compared to a more rigorous simulation approach is presented. The chapter ends by simulating the temperature response of the simulated CNT films, the temperature simulation model is introduced, and the simulated results are compared with experimental results of the CNT films. Finally, chapter 4 provides the conclusive summary of the developed hypothesis and its broader applications being beyond CNT films, the chapter then continues to acknowledge the limitations that the author had to face and the assumptions that had to be made in order to overcome it; the justification for all the assumptions are presented. Finally, the thesis ends by presenting the future work that can be developed based on the current understanding of the developed hypothesis.

Chapter 1: Literature Survey

The literature survey will begin by providing a few individual examples of existing literature work on passive radiative cooling and heating applications, followed existing mechanochromic materials, their classifications and their applications as smart thermoregulating materials.

The first successful application of daytime radiative cooling of a surface directly exposed to solar radiation was first demonstrated by Raman *et al.* [6], where they achieved a surface temperature of nearly 5℃ below ambient temperature. The radiative cooler was designed by integrating a silver backed surface with a Bragg reflector consisting of seven alternating layers SiO_2 and HFO_2 with varying thickness. The integrated design reflected 97% of incident solar radiation while strongly emitting in the atmospheric transparency window. In the preceding years the concept of Raman was further made more applicable and practical by Yang et al with the development of a flexible glass-polymer hybrid metamaterial radiative cooler [7]. The flexible cooler was designed by embedding glass microspheres randomly in a polymer matrix, the resulting design demonstrated an infrared emissivity greater than 0.93 across the atmospheric transparency window while maintaining full transparency in the solar radiation spectrum, thus when backed with a silver coating, a high reflectivity in the solar region can achieved. Due to the random distribution of microspheres, the work of Yang is more manufacture friendly compared to the stricter nano-fabrication requirements of the Bragg reflector of Raman. However, both these publications require the use of precious metals such as silver for increased solar reflectivity. The work of Yang was further improved by Nie et al by the introduction of hollow glass spheres in a PDMS matrix [8].

The addition of hollow spheres provided inherent high reflectivity in the solar region, without the need for a silver backing while maintaining high emissivity in the transparency window. Shown in figure 5 are the schematics of the radiative cooler references 6 and 7 respectively.

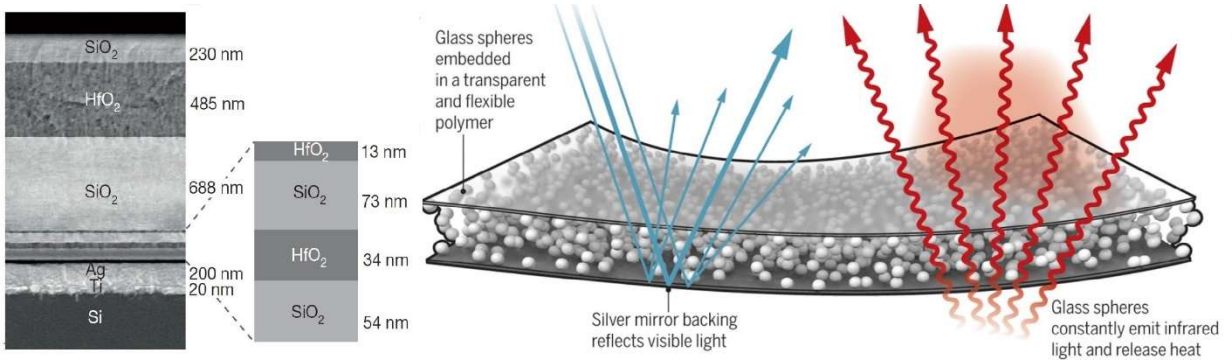

Figure 5: Schematic of multilayered structure [6] (left) and glass-polymer hybrid metamaterial [7] (right)

The design of optimized surfaces for the absorption of solar radiation is comparatively easier than a radiative cooler, thus in this literature review references will not be extensively explained. Some of the optimized solar heaters in literature include the use of metal dielectric multilayered structures [9], nano textured surfaces [10] as well as the combination of both multilayered and textured nano structures [11].

The work presented thus far in this literature review consisted of materials with static optical properties. Hence, resulting in static thermal responses, the design of materials with dynamic optical properties are of higher interested since there is an associated change in response. May it be a thermal, visual or other, this change in response can be used in applications such as sensors to smart materials; responsible for regulative properties such as thermoregulation etc. Materials capable of changing their optical properties due to different stimulus inputs can be classified as electrochromic, thermochromic and mechanochromic materials. In this review only mechanochomic materials are discussed.

A mechanochromic material is a material that exhibits a change in radiative properties due to induced mechanical forces such as pressure, strain, shearing etc. This change in optical properties can result from chemical and physical changes across varying length scales ranging from a few nanometers; determining the molecular arrangements, to distances up to a few micrometers between suspended particles/layers [12].

These chemical examples include mechanophore polymers; chemical reactions triggered by mechanical forces giving rise to change in optical properties [13] these types of mechanophores are used in the medical industry for oxygen and PH level monitoring [14] and the food packing industry to identify damaged goods [15] and even used in novel 3D printing applications as well [16]. Literature work on change in physiology driven mechanochromics materials include photonic gels; these work on the principle of thin film interference. Photonic gels can be described as photonic crystals with thin layers of different materials embedded in a soft gel matrix, as the composite material is strained or swelled by a reagent the layer spacing changes resulting in a different optical property [17] these types of gels have found application in the medical industry for the detection of specific viral strains [18]. In this brief literature survey, it can be stated that the operating mechanism of photonic gels is the most similar mechanism to the work presented here in this thesis.

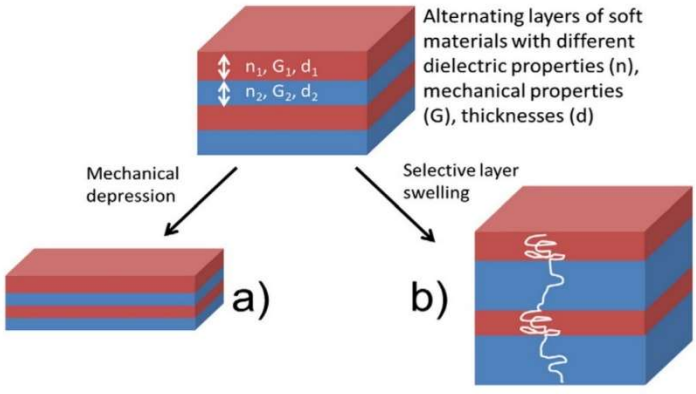

Figure 6: Schematic of a 1D photonic gel [12]. (a) Under mechanical compression. (b) Swelling due to reagent

In this literature survey it was found that while mechanochromics are extensively used in the medical industry for the manipulation of visible light, the use of mechanochromics in thermal applications lacks a similar interest. A few of the literature work on the dynamic manipulation of radiative properties in the near to mid IR wavelength range include the use of strain driven corrugated crumpled nickel as personal flexible thermal regulator for wearables [19] and mechanical reconfigurable work on graphene, capable of broadband band emissivity control from UV to mid IR [20], both these publications are the works of Krishna *et al.*

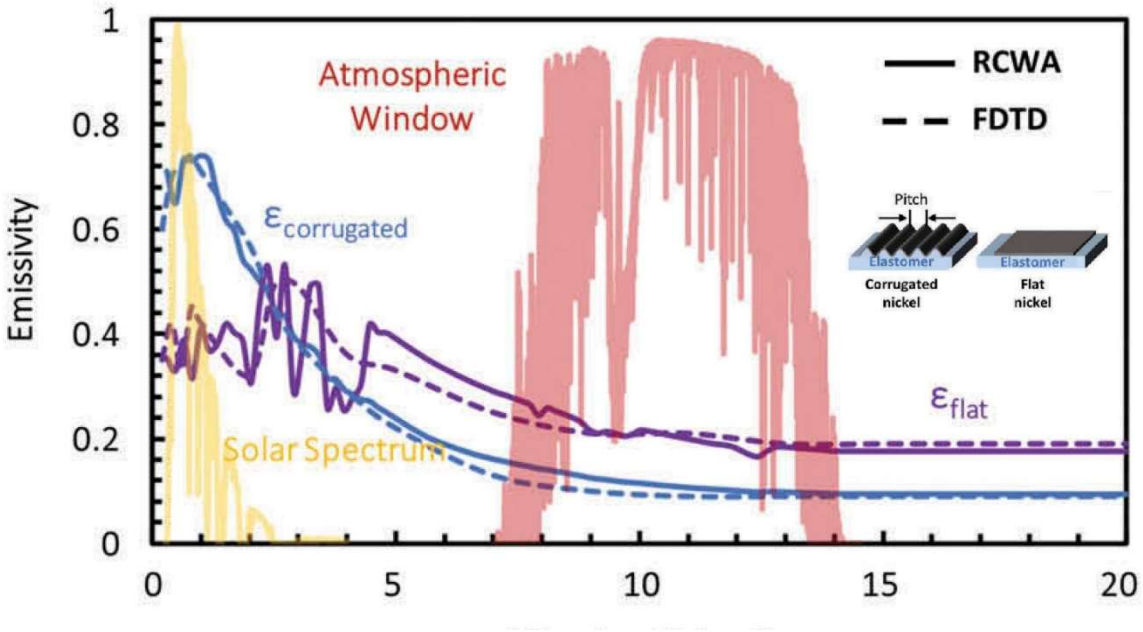

Figure 7: Emissivity plot of corrugated nickel vs. flat nickel [19]

The first work of Krishna in reference 19, involves the evaporative deposition of a thin film of nickel on a pre-strained polymer, as the polymer is relaxed and allowed to return to its normal unstrained state, the deposited nickel forms nanoscale periodic corrugations. This surface morphology change results in the absorptivity of nickel to change from an average value of 0.3 to 0.7 in the 0.2 - 2.5 μm wavelength range, resulting a temperature response change of nearly 10℃. The work of reference 20 is similar to that of 19, and thus will not be discussed in detail in this review.

The development of a mechanochromic smart material for thermoregulation purposes requires two aspects; a material capable of exhibiting a change in optical properties due to a mechanical stimulus and an input stimulus to cause needed change. To provide the needed input stimulus an actuating mechanism as well as a sensor to determine the needed degree of actuation is needed.

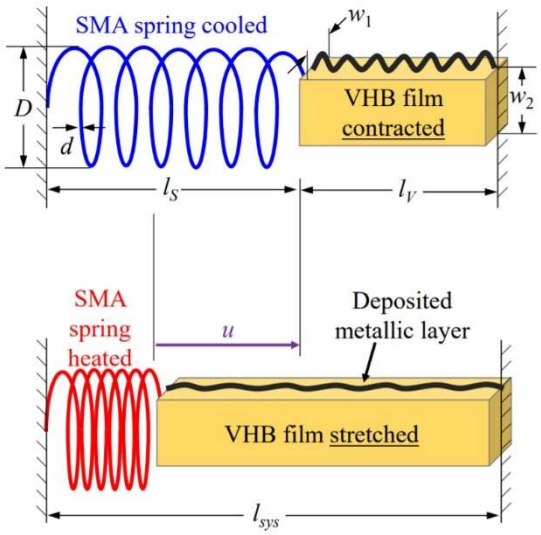

Figure 8: Schematic of series connect SMA and nickel deposited VHB [21]

The work by Hernandez *et al.* [21] builds on the work of corrugated crumpled nickel by Krishna, the natural elasticity of the nickel deposited polymer was coupled with a shape memory alloy (SMA) spring in series as shown in figure 8. SMA is a smart material capable of generating temperature driven actuation strain, this allows the material to recover from moderate mechanical deformations, allowing the material to exhibit what is known as shape memory. Thus, in the SMA spring functions as both a sensor and an actuator. When the system temperature rises due to incoming solar radiation the SMA spring contracts stretching the crumpled nickel, reducing its solar absorptivity causing a temperature drop, as the temperature drops in the system, the SMA relaxes and the nickel becomes more absorptive again. This repetitive process continues and allows the system to maintain a constant temperature range in completely passive manner.

Chapter 2: Experimental Work

Note the work presented in this chapter are not the work of the author of this thesis. The chapter was included to educating the reader on how CNT films were fabricated, its strain-dependent optical properties and how these properties would manifest as a thermal response. All experimental measurements and characterizations of CNT films were carried out by my lab mate Xiao Nie from the NTER lab here at University of California Irvine. The CNT film samples were synthesized and provided to the NTER lab by Professor Choongho Yu in Texas A&M University.

2.1 Fabrication Procedure

A brief explanation of the polymer coating procedure used by Dr. Choongho Yu is provided in this section. First the CNT sponge like structure shown in figure 9a is synthesized using chemical vapor deposition (CVD) [22], later this CNT sponge is coated with a thin film of eco-flex [23]. This secondary coating procedure is implemented to ensure large strains under repeated cycles; in the order of thousands. This structural enhancement provides the ability to strain the new CNT sponge driving the observed optical changes.

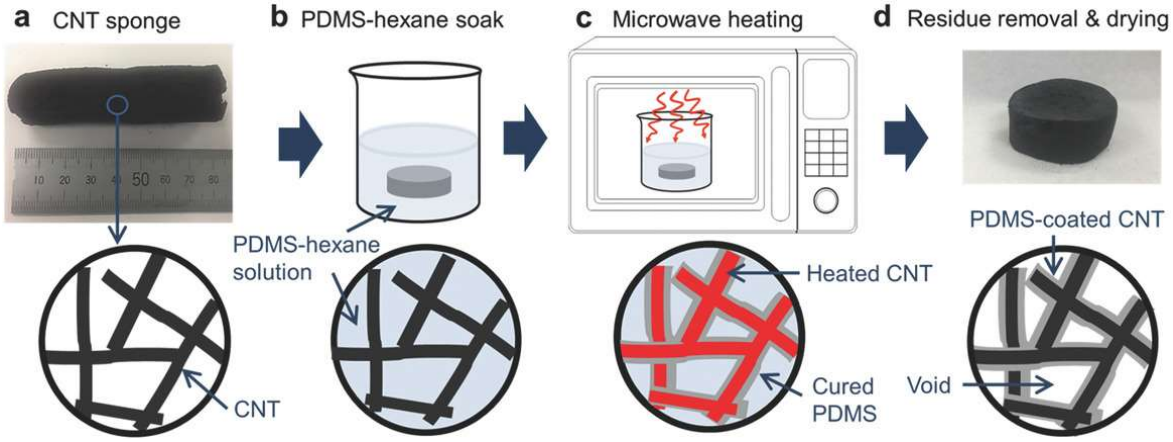

Figure 9: Fabrication procedure of polymer coating. Note PDMS was substituted with eco-flex in the samples used in this thesis [23]

As the first step 3 wt. % of eco-flex is mixed with hexane and left for 1 hour for sonification, after wards the CNT sponge is immersed in the mixture and stirred for two hours allowing the mixture to thoroughly penetrate in to the porous. Once fully soaked the entire beaker with the sponge is exposed to microwave radiation for 3 seconds at 450 W via the use of a 900 W microwave oven at 50% power. Radiation exposure is repeated 5 times while allowing for natural cooling for around 10 – 15 seconds. Microwave radiation allows the ability to selectively cure the eco-flex near the surface of the CNTs, this is due to CNTs strong absorptivity in the microwave wavelength length range, this causes the CNT to achieve localized heating compare to the rest of the mixture and the beaker, allowing for localized curing. After radiation exposure the excess uncured eco-flex is dissolved in pure hexane, resulting in an eco-flex coated CNT sponge. Finally, the coated CNT sponge is compressed on to an eco-flex substrate as shown in figure 10, providing the platform for stretchable CNT films.

Figure 10: Samples prepped with eco-flex substrate for straining

2.2 Optical Property Measurements

The optical properties of the CNT films were measured in the spectral range of 0.2 μm till 2 μm; corresponding to the solar radiation spectrum. The optical properties of the strained and unstrained CNT samples in the UV, visible and near-infrared (NIR) region are characterized by Ultraviolet-Visible-NIR (UV-VIS-NIR) spectrometer; Cary 7000 by Agilent and Jasco V670 by Jasco Technology were used to measure the transmissivity and reflectivity respectively. In the reflectivity measurement a 60 mm integrating sphere was used. The diffuse reflectivity measurements were calibrated with a standard white body.

Figure 11: CNT measurement locations (left) and Stretched CNT film set up (right)

The CNT film was stretched and tightly taped on both sides with a black tape and attached to the ends of a microscope slide to keep it in place as shown to the right of figure 11. Optical measurements were made at 3 different points within the CNT sample and the final results are presented as the average of all three measurements, this was done so to capture the overall optical properties of the sample as a whole.

Three CNT film samples were provided by Dr. Choongho Yu, shown in figure 12 is the strained vs. unstrained reflectivity of one of the samples, note all sample measurements exhibit a similar trend. Since the attempt of this thesis is to explain the strain-dependent reflectivity, here only the reflectivity measurement is shown.

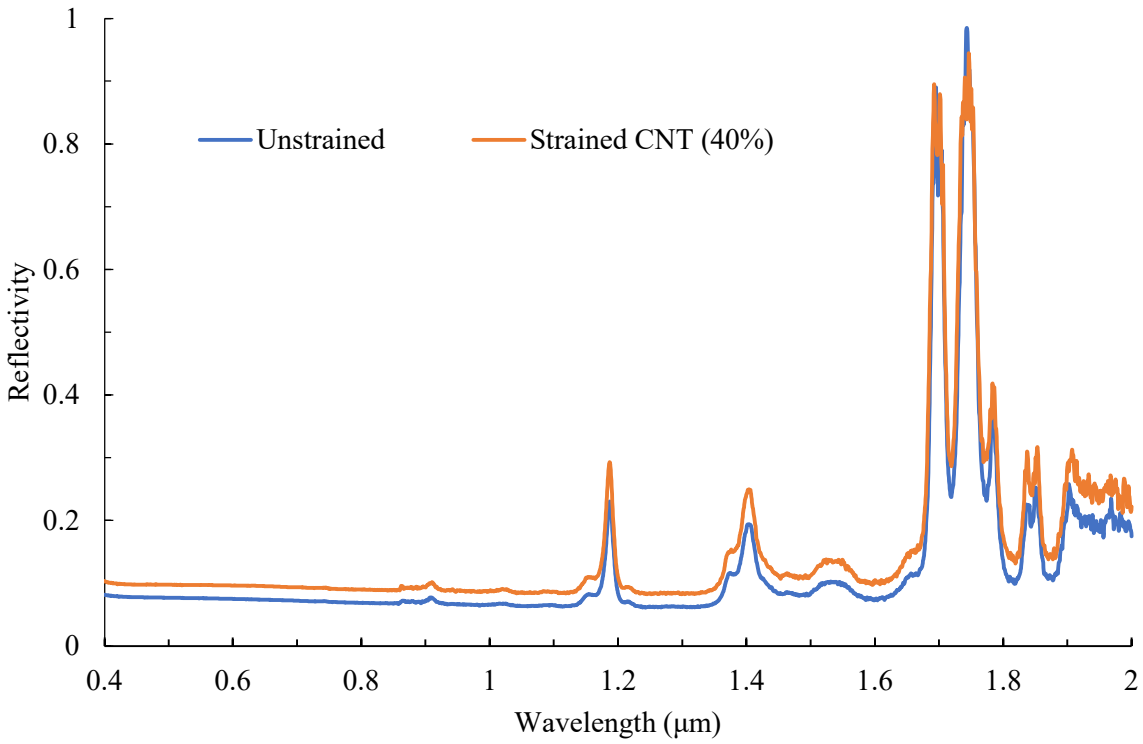

Figure 12: Reflectivity of strained vs. unstrained CNT films

A broadband reflectivity increase is seen between the unstrained vs. strained case; the mean reflectivity increases from 0.1216 to 0.1570. It should be noted that the measurement error of Jasco V670 is ±0.003, with the measurement change at 0.0354 being well above the error range of the instrument.

2.3 Outdoor Temperature Measurements

The outdoor measurements were made on September 4th, 2018; a sunny cloudless day allowing for maximum solar radiation absorption. The temperature measurements were performed on the rooftop of Engineering Gateway at University of California, Irvine where the samples were maintained undisturbed throughout the measurements. Temperature measurements were taken from noon till 3 pm ensuring near normal incidence of radiation. The temperatures of the samples and ambient air were measured by a K-type thermocouple with a resolution of 0.1°C with an inherent measurement uncertainty of ±1.1°C at a temperature range from 0°C to 55°C. A mechanical clamp was used to hold the CNT samples, to minimized thermal conduction from the rooftop to the clamp, it was placed in a polystyrene petri dish supported by three isolation legs. Temperature measurements plot is available in section 3.8.

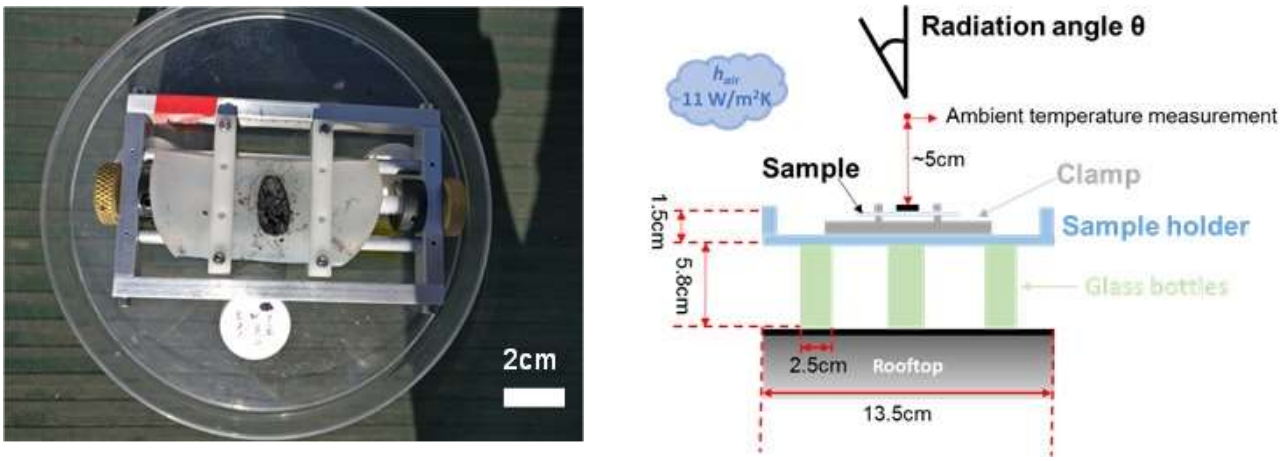

Figure 13: Experimental setup (right) and Schematic of setup (left)

Chapter 3: Computational Work

Note all work presented in this chapter are the work of the author of this thesis, expect for SEM images of CNT films captured by Xiao Nie.

3.1 Modeling of CNT Films

Using the SEM images of CNT films as reference a 3D model was developed in MATLAB. The model was developed to capture the dynamic nature experienced by the CNT films on stretching. The model was designed with a Poisson's ratio 0.5, thus as the model is strained in an axial direction a corresponding negative lateral strain is applied in the axial cross section governed by equation 2. Where d is the original diameter, Δd the change in diameter, L the initial length of the fiber, ΔL the change in length caused due to straining and ν the Poisson's Ratio.

$$\Delta d = -d\left(1 - \left(1 + \frac{\Delta L}{L}\right)^{-\nu}\right) \qquad \text{Eq. 2}$$

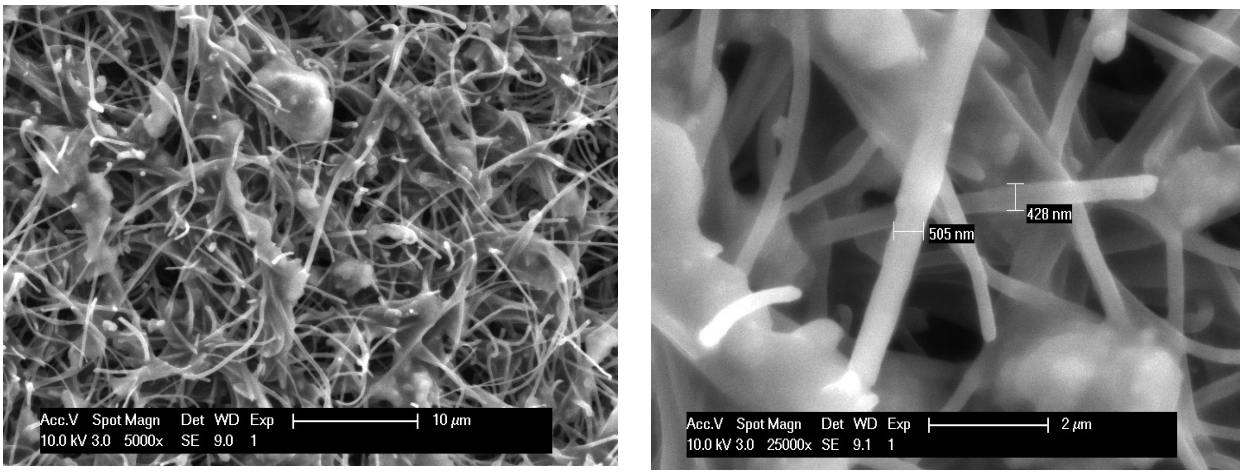

Figure 14: SEM image of CNT film (left) and Zoomed in image (right); courtesy of Xiao Nie

The diameter and the length of all the fibers in the model was set at 500 nm and 12.5 μm respectively, however each wire was allowed to change direction randomly 5 times at equally spaced distances as shown in figure 15a, providing the ability to create different fiber geometries. The location of each fiber was determined randomly, thus the fibers were allowed to overlap. The overlapping of fibers provides the possibility of recreating the complex structure seen in figure 14, the work of similar 3D models in literature include [24]. The 3D model shown in figure 15 was constructed using 250 fibers confined to a cubic unit cell of side 10 μm. It should be noted that the unit cell is set to be periodic in the X and Y directions.

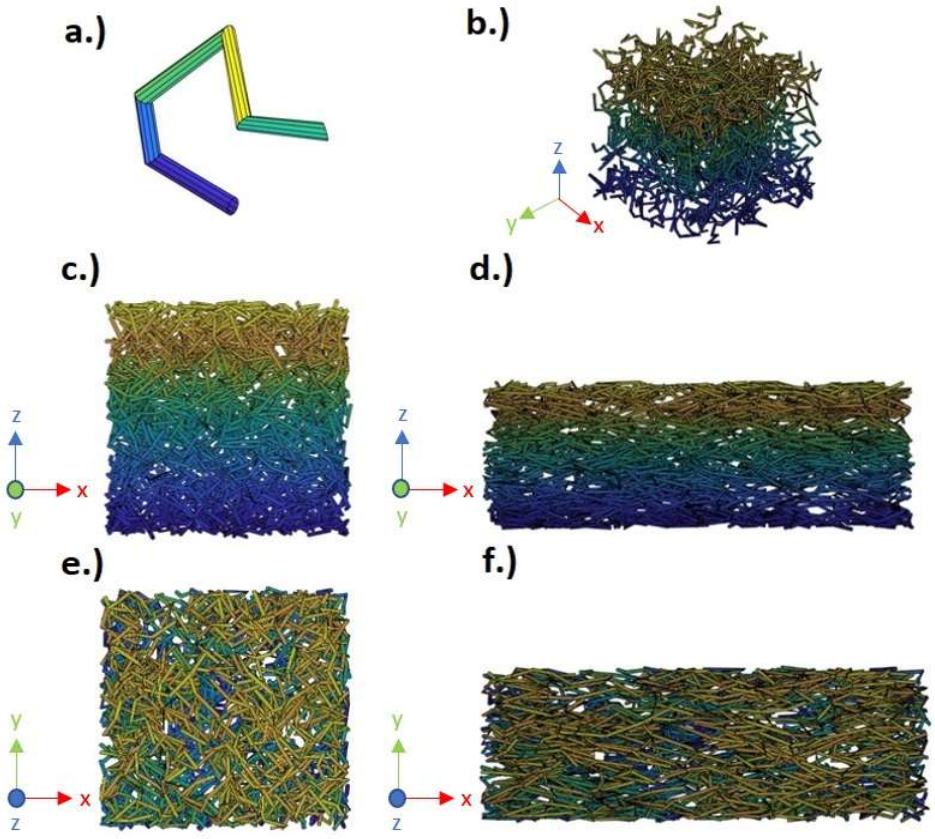

Figure 15: MATLAB 3D schematic of CNT films, Note all strains shows are at 100% strain, a fiber color scheme is used to present the relative location of a fiber in the direction Z a.) Single fiber representation b.) 3D arrangement of all the fibers in 3D space c.) Side view of unstrained case d.) Side view strained case e.) Top view of unstrained case f.) Top view strained case.

3.2 CNT Film Expansion Modelling

The arrangement of the polymer coated CNT is determined by a series of six different points. A circular wire of diameter 500 nm is feed into the trajectory formed by connecting the six points in 3D space. It is these points which are moved when the model is strained, as the points are moved the trajectory is redrawn and the wire is fed again into the new trajectory. This method ensures that the diameter of the polymer coated CNT remains unaffected. However, there is the drawback of artificial linear expansion/contraction of the polymer coated CNT. This linear expansion and contraction are justified by the case of unraveling of clumped up CNT fibers (as seen in the SEM images) and clumping of CNT fibers respectively. The scaling factors of X, Y and Z positions of the points are determined by equation 2. In the case of 100% strain along the X axis, all points in the X direction are scaled by 2 and the all the points in Y and Z are scaled down to 0.7 times the original spacing; this value is governed by Poisson's ratio. Note arbitrary units were used as a reference in figure 16.

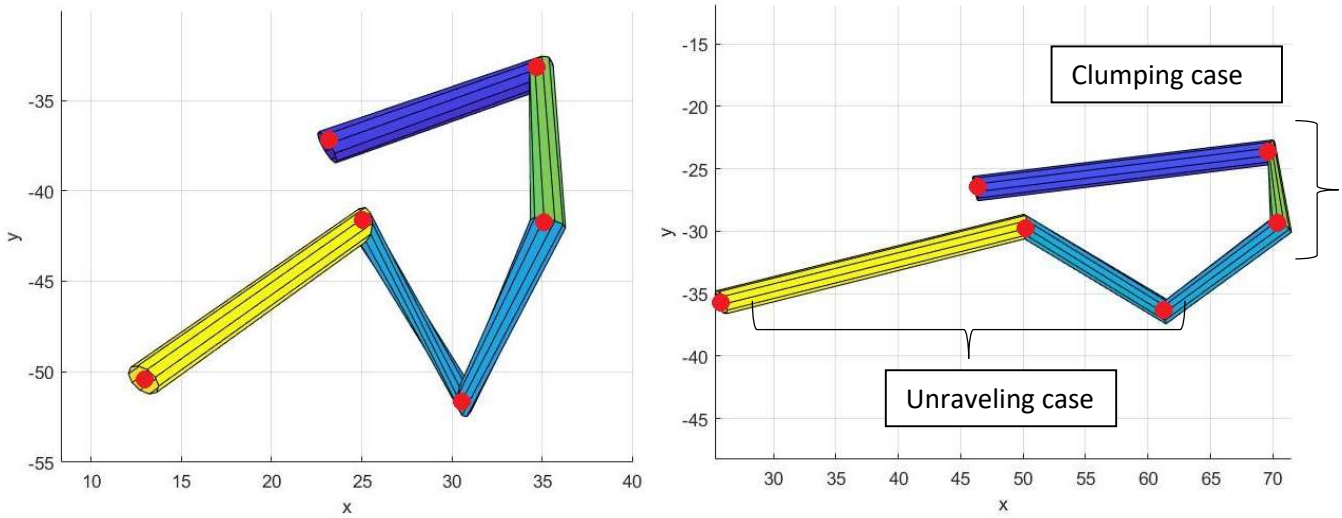

Figure 16: Expansion/Contraction mechanism of CNT; Unstrained fiber (left) and Strained fiber (right)

3.3 Simulation Method: Raytracing

Raytracing was chosen as the preferred method of simulation for the explanation of strain-dependence of reflectivity. This decision was made on account of the complexity of the simulating structure. Simulation of complex structures such as CNT films using rigorous solvers such as FDTD and RCWA are not computationally feasible due to the strict discretization requirements imposed by them. Thus, the less computationally intensive method of raytracing was adopted for the work on this thesis. Compared to the previous two methods which uses the explicit wave nature of Maxwell's equation for calculation of optical properties, raytracing approximates the wave nature of EM radiation as a particle/ ray and uses geometric optics to simulate the materials response to radiation. It should be noted that the raytracing scheme can be appropriately modified to successfully simulate complex wave phenomena such as diffraction, polarization and thin film interference [25-27]. Raytracing simulations are generally considered valid as long as $\frac{\pi d}{\lambda} > 100$, however this condition is a broad universal generalization, thus accurate comparable results can be achieved under lower constrains; discussed more in detail in section 3.6. Raytracing model used in this thesis was based on the work of Hyers *et al.* [28] which used the condition $\frac{\pi d}{\lambda} > 1$.

Most EM simulation schemes requires the refractive index of the material as an input, however the particular model of raytracing used in this thesis requires the input properties of the materials to be in terms of absorptivity, reflectivity and transmissivity. These specialized input values are first obtained by using RCWA by simulating a slab of graphite at a thickness of 500 nm, which corresponds to the diameter of CNT fibers in the model.

Note in this thesis the material assignment to CNT films for simulation purposes is graphite [29], this decision was made due to the lack of measured refractive index availability of CNT/graphene in the desired spectral range. Note n is the refractive index and k is the extinction coefficient.

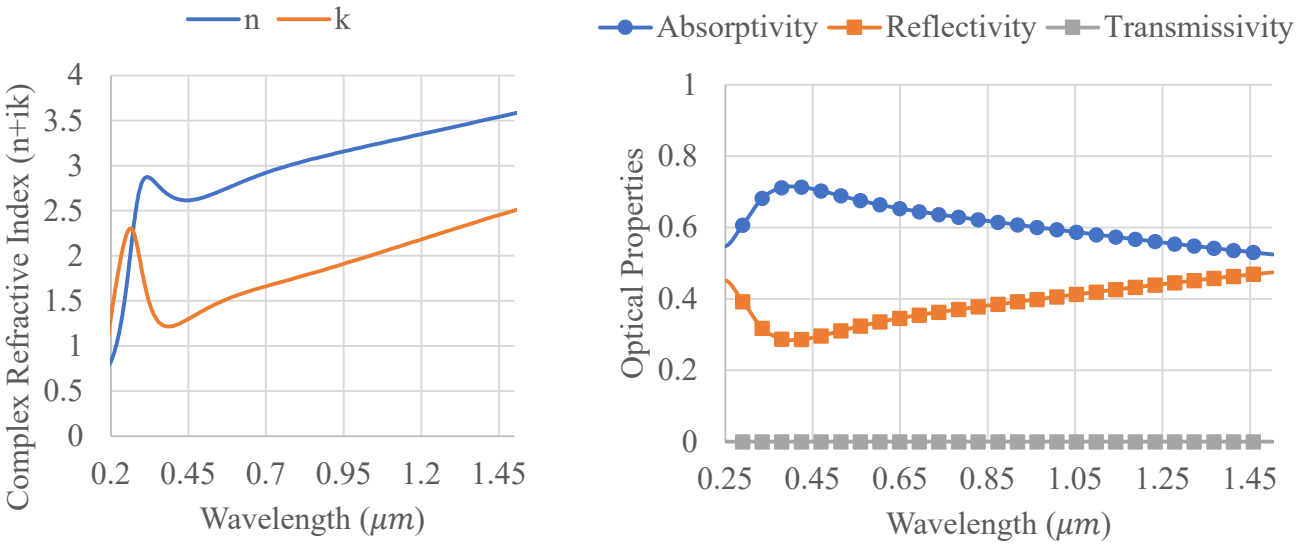

Figure 17: Obtaining material input parameters for raytracing; The n,k values of graphite (right) are converted to absorptivity, reflectivity and transmissivity (left) by using RCWA.

Note the hypothesis of the mechanism was initially explained using the spectral range 0.2 μm till 1.5 μm, later this will be extended till 2.5 μm to perform the temperature simulation analysis. For the extended inputs the same procedure highlighted in figure 17 was used.

Raytracing is a Monte Carlo procedure, that uses a large sampling of randomized cases to obtain deterministic results [28,30,31]; in this simulation 50,000 photons were shot (per wavelength/frequency). All photons were shot normal to the yellows surface shown in figure 18. The origin location of the photon was chosen randomly within the yellow surface. Note all surfaces the photon strikes is considered to be optically thick, thus no transmission of photons through the surface material is considered; in order for this assumption to be valid the input material properties for raytracing should exhibit a optically thick (transmissivity = 0) nature as shown in figure 17.

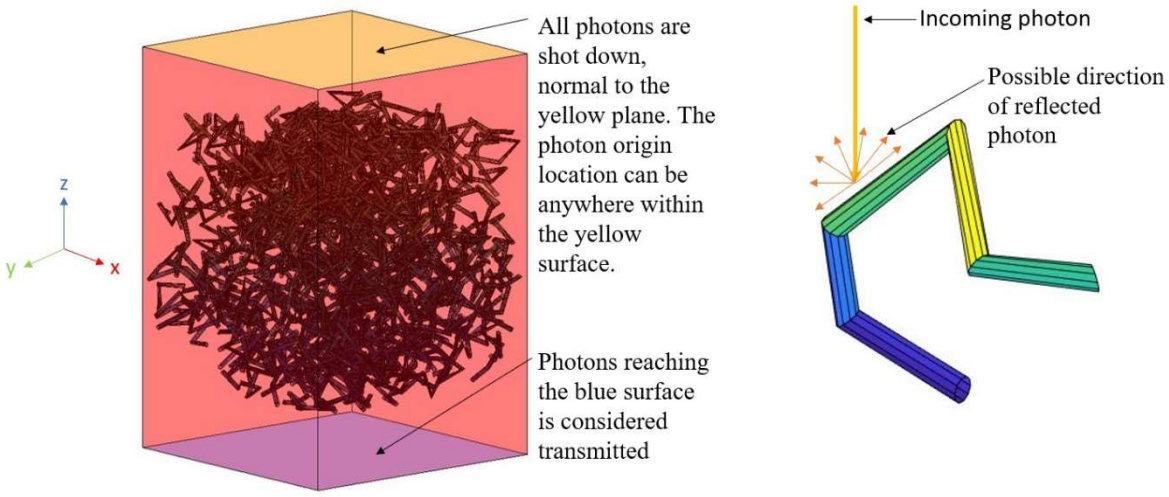

Figure 18: Raytracing simulation setup (left) and how new reflected direction is determined (right)

Therefore, once the photon strikes a surface it is either reflected or absorbed, whether a photon is reflected or absorbed is determined by the frequency of the photon and the absorptivity of the material at that frequency. Once the photon strikes a surface, a random number is generated between zero and one and that value is compared to the absorptivity of the material it impacted. If the random number is larger than absorptivity of the surface the photon is considered to be reflected.

The new reflected direction of the photon is chosen randomly (representing the diffuse nature of reflection) in a hemispherical direction away from the impacted surface. This procedure is repeated until either the photon is absorbed, backscattered to the yellow plane or transmitted to the blue plane. The backscattered photon is considered a reflected photon and photon reaching the blue plane is considered a transmitted photon; a photon can be directly transmitted (with no collision) or transmitted via a series of reflections. Note the raytracing simulation platform used in this thesis was completely developed from the ground up by the author alone. The detailed mathematical mechanics of raytracing is widely available in literature [32] and hence, will not be discussed in this thesis.

3.4 Strain Sweep Simulation Results

Eight different raytracing simulations were run at a spectral resolution of thirty equally spaced points between 0.2 μm till 1.5 μm, a broadband reflectivity response similar to the experimental results of strained CNT films was observed. Transmissivity of the simulated CNT film was observed to be at near zero values at all strain values; which was expected given the density of fiber packing. Thus, interested readers can find the absorptivity by subtracting reflectivity values by unity.

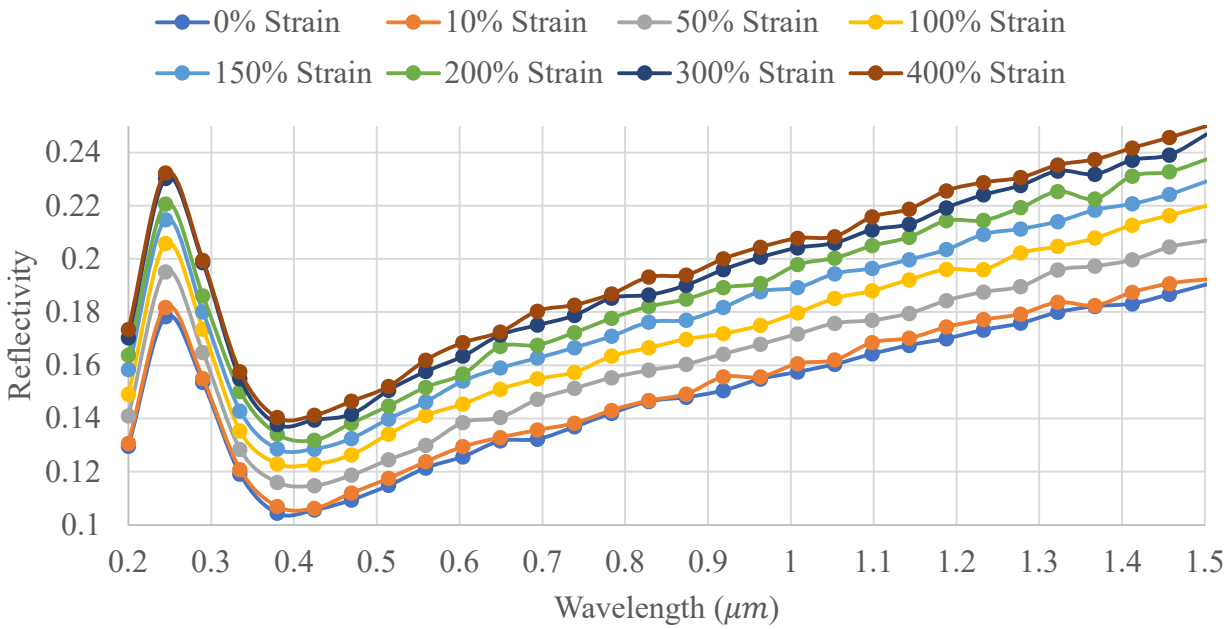

Figure 19: Strain-dependent raytracing results

It is important to note that even though the experimental samples of CNT films were not strained beyond 80%, the samples were simulated to a larger range to capture the broader mechanism behind the strain-dependent reflectivity. In order to observe the trend between reflectivity and strain, the averaged optical properties within the simulated range was compared to the degree of strain as shown to the left in figure 20. A decreasing enhancement of reflectivity with increase strain is observed, with the maximum reflectivity reaching a plateau at higher strain.

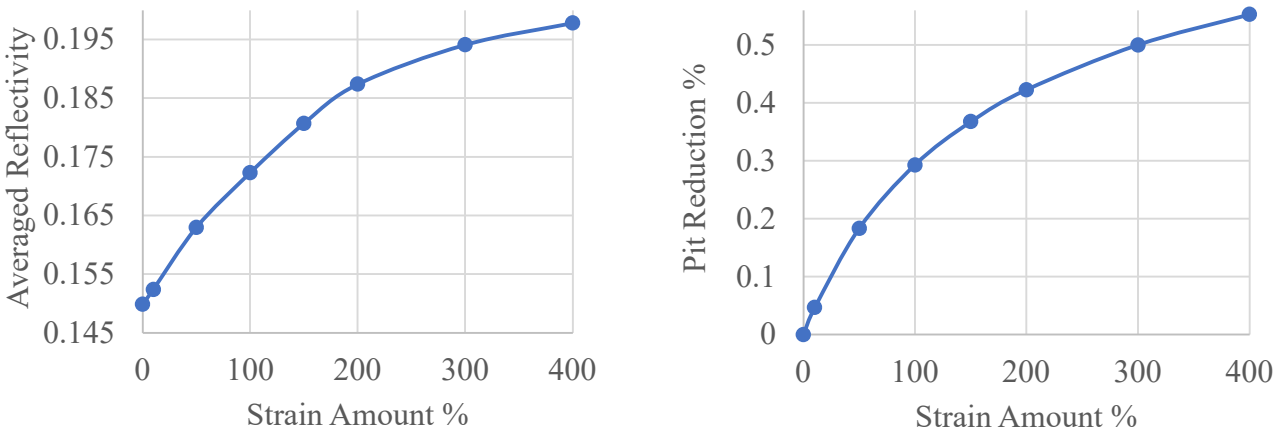

Figure 20: Averaged reflectivity (left) vs. strain and reduction of pit depth vs. strain (right)

A similar trend is observed in the reduction of lateral width (Δd) in (referred to as pit depth) equation 2 with increasing axial strain, shown to the right of figure 20.

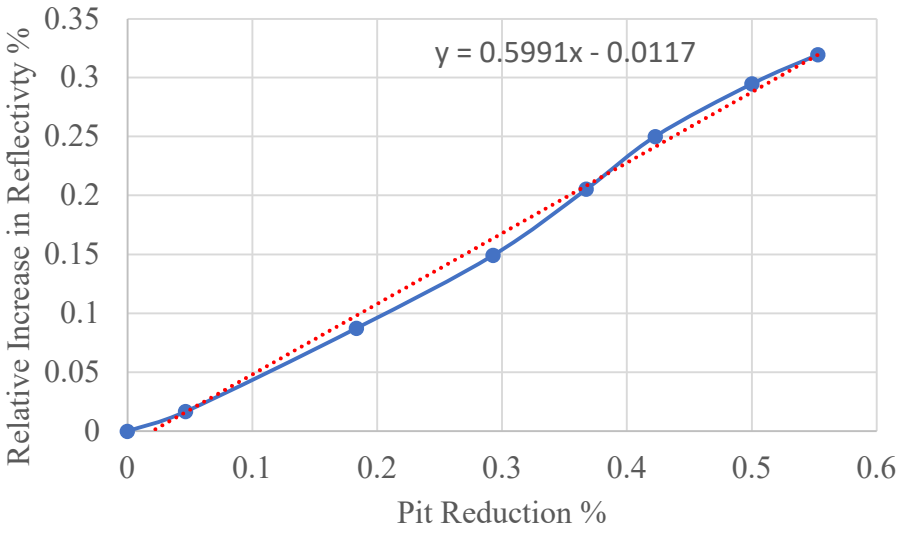

Figure 21: Trend between pit reduction and increase in reflectivity

Once relative increase in reflectivity as percentage is plotted with respect to pit reduction as a percentage a clear linear relationship is observed. Thus, it is believed that the pit reduction caused due to straining plays a critical role in the increase in reflectivity.

3.5 Proposed Hypothesis

The surface of the CNT film can be assumed to be composed of many pits; these pits represent the porous nature of the polymer coated CNT sponge. The simulated path of one photon near the surface is shown in figure 22, it is clear that the behavior of the photon can be attributed to the presence of an imaginary pit near the surface. Note that the photon path shown is not an artistic representation, the path shown is an actual raytraed simulated path of one photon.

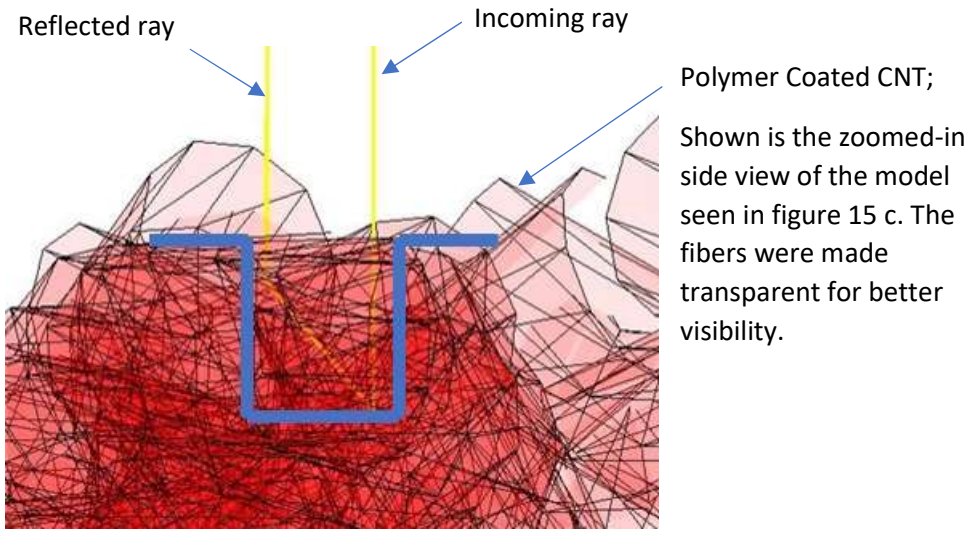

Figure 22: Pit equivalence seen in CNT film model (cross section); shown in yellow is the traced path of one photon and show in blue is the imaged pit structures found on the surface.

As CNT film is strained in the X direction a lateral negative strain is applied to the Y and Z directions. The lateral straining in the Z direction causes the gap between the fibers in the vertical direction to reduce thus causing the "pit depth" to reduce. Allowing more photons to escape the pit by backscatterting.

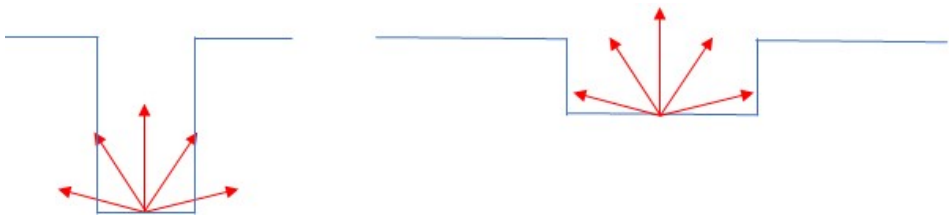

Figure 23: Diffuse reflection in unstrained pit (left) vs. strained pit (right)

It is clear from the unstrained case in figure 23 the chance of a photon escaping the pit with direct reflection is 20% whereas the chance of strained case is at 60%; the chance of indirect backscattering (reflecting again from the walls of the pit) from a pit is comparatively less likely due to the high absorptivity of graphite in the desired wavelength range. Thus, if the hypothesis were to be valid, a significant increase in the number of direct reflections (backscattering with just one collision) with increasing strain should be visible.

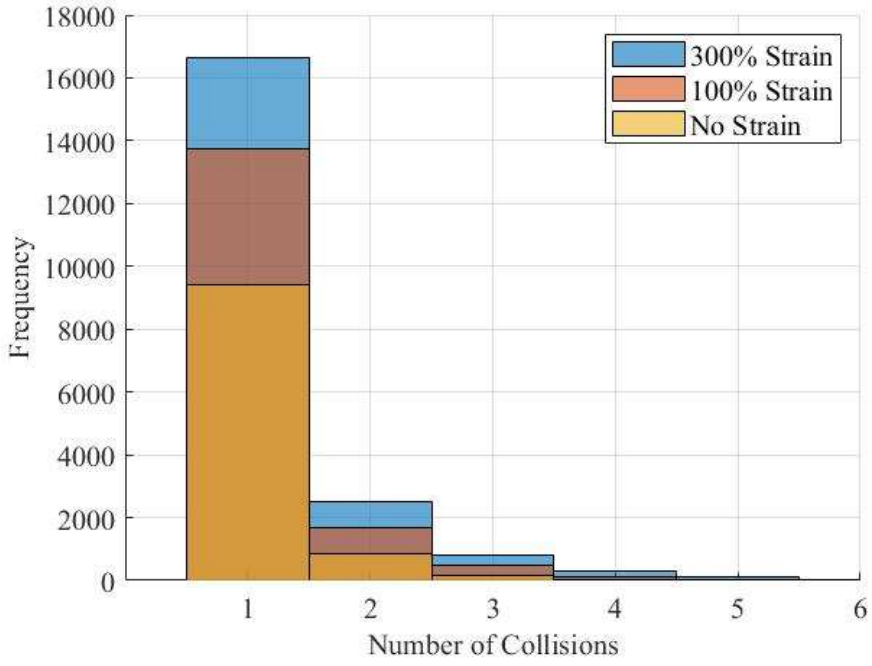

Figure 24: Tabulated number of collisions before backscattering in raytracing simulations

From figure 24 it is apparent that enhancement of reflection due to straining is caused by the increase of direct reflections and higher strain is shown to cause this increase in reflected particles as seen from the histogram. Thus, this figure serves as a confirmation of the validity of the proposed hypothesis.

3.6 Validity of Raytracing

As mentioned before in section 3.3 raytracing simulations are generally considered valid as long as the size parameter; $\frac{\pi d}{\lambda}$ is greater than 100 [33]. However, this is a broad generalization, thus the accuracy departing size parameter for raytracing needs to be analyzed on a case by case basis. In the simulation shown before the averaged size parameter was calculated to be at 2.61. The motivation of this section is to compare raytracing with a rigorous solver such as RCWA to confirm if the raytracing is capable of capturing the trend of the averaged reflectivity vs. strain demonstrated by a rigorous solver. However, solving the current CNT film model in RCWA is not practical due to the solvable geometry limitations imposed by RCWA. Thus, a new simpler model was designed representing the complex nature of the CNT film. The schematic of the new model is shown in figure 2.

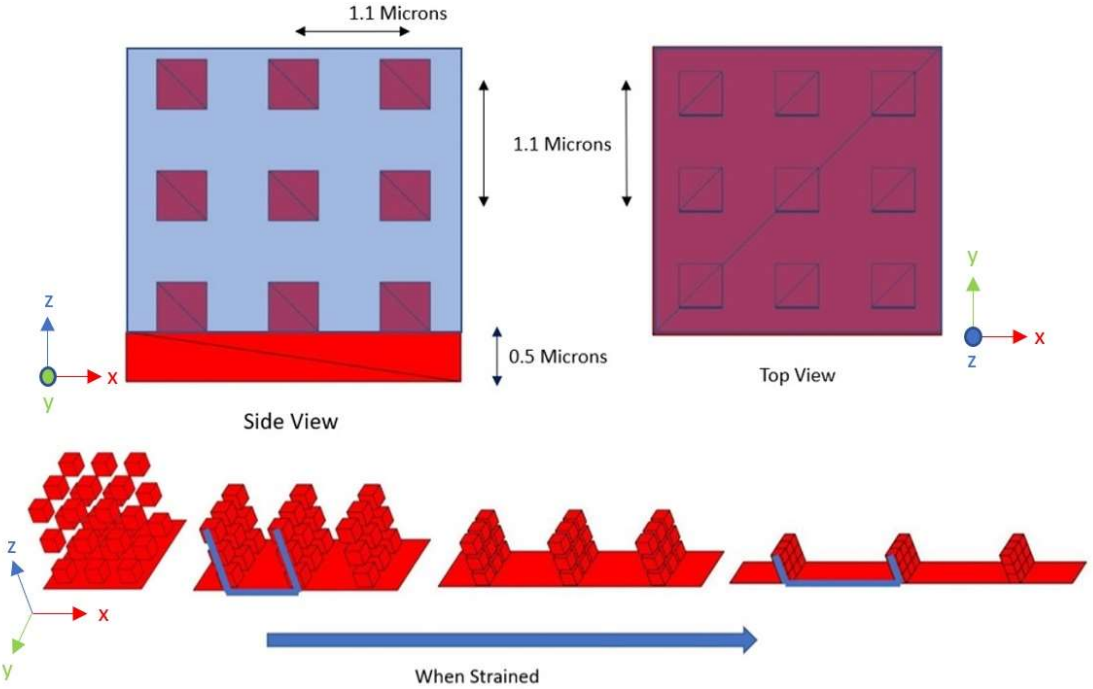

Figure 25: Shown on top, the schematic of the simpler comparison model, shown below is how the model would behave when strained, the behavior was modelled based on the concept of pit depth.

The simpler comparison model consists of graphite cubes of side 500 nanometers (representing the diameter of the CNT) arranged in a cubical fashion in 3D space, each graphite cube is spaced from one another at a distance of 1.1 μm from all three-dimensional directions as seen in the topmost images of figure 25. The model is made to be infinitely periodic in the X and Y directions, and finite in the Z direction with only three layers of graphite cubes in the positive Z direction. The cubes are embedded in a stretchable polymer with a Poisson's ratio of 0.5, for simplicity of simulation the polymers material was assigned to that of air; this assumption is valid for the interested spectral range of solar radiation since most polymers such as PDMS exhibit very high transmissivity in this region. Finally, the graphite cube embedded polymer is kept on a 500-nanometer graphite substrate that does not take part in straining.

The displacement of the graphite cubes are governed by equation 2, the initial spacing of the graphite cubes in the unstrained case was strategically spaced in order to achieve completed contact between the cubes in the directions of Z and Y at maximum strain (400%). Note the simple comparative model was specifically designed to mimic the proposed mechanism in section 3.5, the widening and shallowing of the imagined pit depths are shown in blue in the lower image in figure 25.

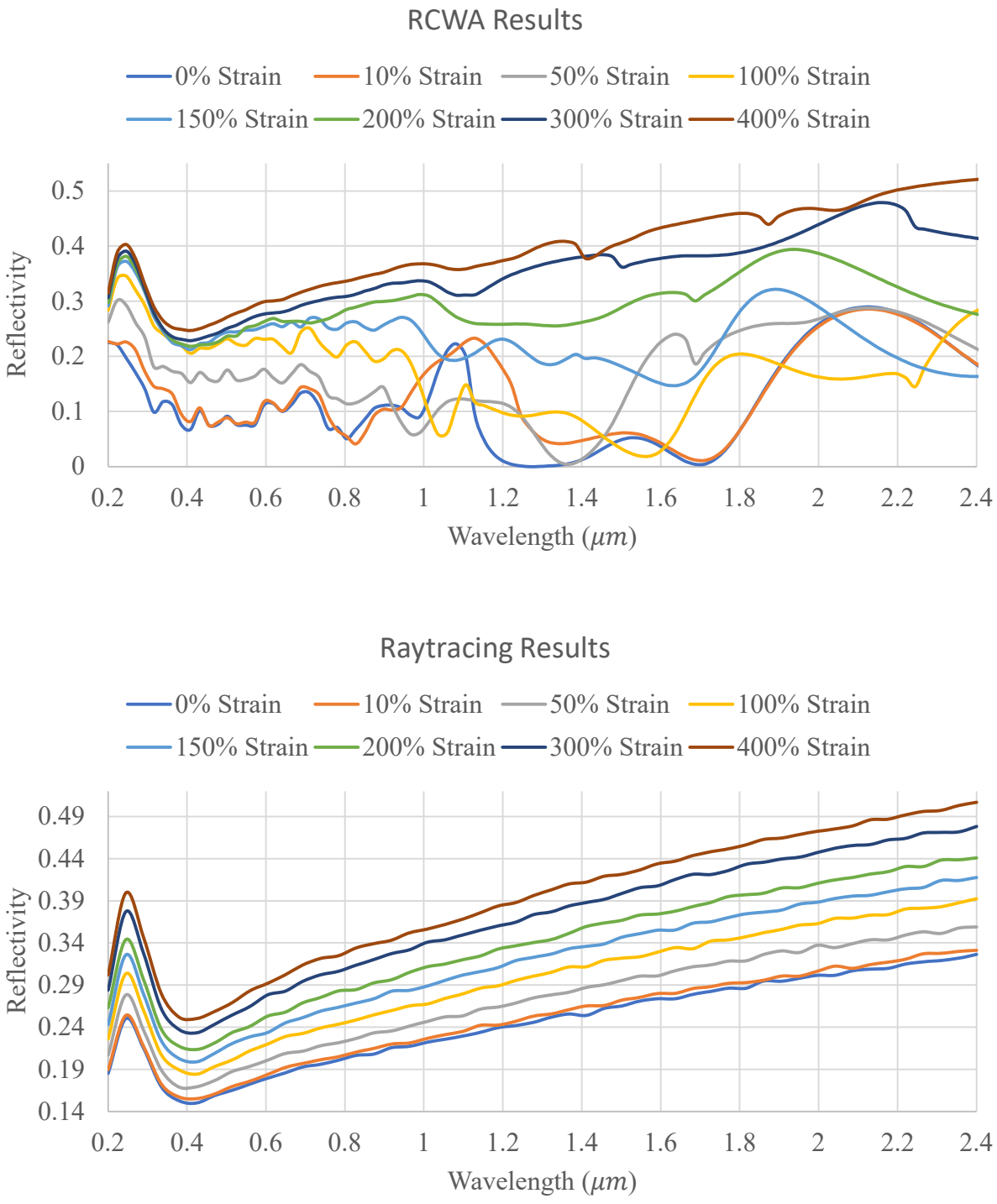

Figure 26: Comparison of RCWA (top) with Raytracing (bottom)

From figure 26 it is clear that RCWA is capable of capturing a more spectrally complex behavior of reflectivity at different levels of strains compared to raytracing.

However, in this thesis goal is to explain the averaged reflectivity dependence with strain thus the plots shown in figure 26 was averaged for the entire solar spectral range.

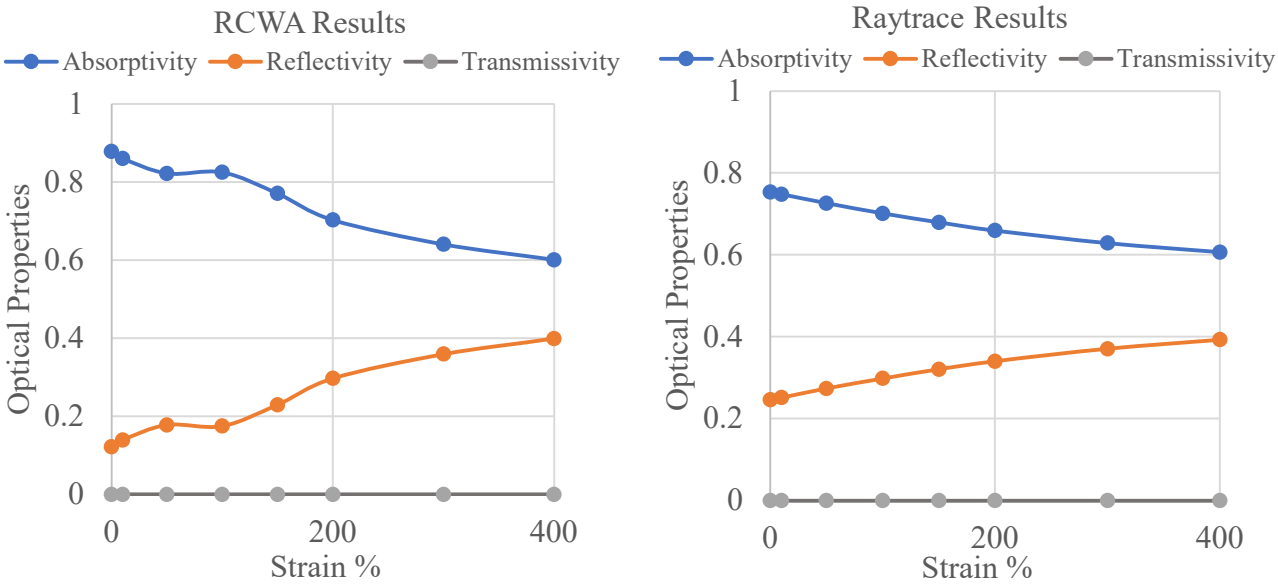

Figure 27: Comparison of averaged optical properties; RCWA (left) and Raytracing (right)

Once the spectral results in the solar region are averaged, a close resemblance between the two simulation mechanisms is seen. Simulation results are seen to become more comparable to each other at increasing strains; the largest deviation in the results are seen at the unstrained case and both the simulations results being nearly identical in the maximum strained case. The improving accuracy of raytracing is attributed to the increasing size parameter with increasing strain. Thus, from this comparative analysis it can conclude that the use of raytracing in the development of the hypothesis in section 3.6 can be considered valid since the trend is successfully captured.

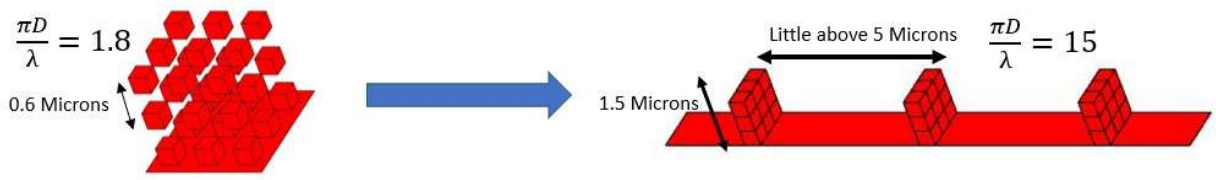

Figure 28: Variation of size parameter with increasing strain

3.7 Temperature Prediction Model

The steady state temperature (T) of the CNT film is calculated by using the power balance shown in equation 3. The power input to the system includes both the incident solar radiation (P_{sun}) and the atmospheric radiation from the surrounding air (P_{atm}), the power losses are due to the thermal radiation emitted from the sample (P_{rad}) and the parasitic loss of power due to conduction and convection lumped in to one term as (P_{loss}).

$$P_{rad}(T) - P_{atm}(T_{amb}) - P_{sun} + P_{loss}(T, T_{amb}) = 0 \qquad \text{Eq. 3}$$

P_{rad} is calculated by multiplying the blackbody radiance ($I_{BB}(T, \lambda)$) with the simulated surface emissivity values of the CNT (ε_{CNT}) integrated over a hemispherical dome, as shown in equation 4. Note the emissivity values beyond 2.5 μm in CNT film was calculated using RCWA by assuming the entire CNT film as slab of graphite of thickness 500 nm. This assumption is valid since the dominance of size effect by the pores of CNT films become less significant at longer wavelength ranges.

$$P_{rad}(T) = A \int \cos(\theta) d\Omega \int_0^{\infty} I_{BB}(T, \lambda) \varepsilon_{CNT}(\lambda, \Omega) d\lambda \qquad \text{Eq. 4}$$

$$where \qquad I_{BB}(T, \lambda) = \frac{2hc^2}{\lambda^5 (e^{\frac{hc}{\lambda k_b T}} - 1)} \qquad \text{Eq. 4. a}$$

$$and \qquad \int d\Omega = \int_0^{\pi/2} \sin(\theta) d\theta \int_0^{2\pi} d\emptyset \qquad \text{Eq 4. b}$$

Equation 4a and 4b represents the blackbody radiance and the angular integral over a hemisphere respectively. Where A is the area of the surface, λ the wavelength, Ω the solid angle, θ the polar angle and $\emptyset$ is the azimuthal angle.

P_{atm} is calculated similar to P_{rad} with the exception of replacing ε_{CNT} with $\varepsilon_{CNT} * \varepsilon_{atm}$. where t is the atmospheric transmittance along the zenith.

$$\varepsilon_{atm}(\lambda, \Omega) = 1 - t(\lambda)^{1/\cos(\theta)} \quad \text{Eq. 5}$$

The incident solar power P_{sun} is calculated by multiplying AM 1.5 [4] with the extended simulated emissivity values of CNT as show in equation 6.

$$P_{sun} = A \int_0^{\infty} I_{AM1.5}(\lambda) \varepsilon_{CNT}(\lambda) d\lambda \quad \text{Eq. 6}$$

Finally, the loss of power due to the conduction and convection (P_{loss}) is calculated using a combined effective heat transmission co-efficient h_{ef} set at a value of 11 $Wm^{-2}K^{-1}$. Where P_{loss} is written as shown in equation 7.

$$P_{loss} = Ah_c(T_{amb} - T) \quad \text{Eq. 7}$$

3.8 Simulated Temporal Temperature Profile

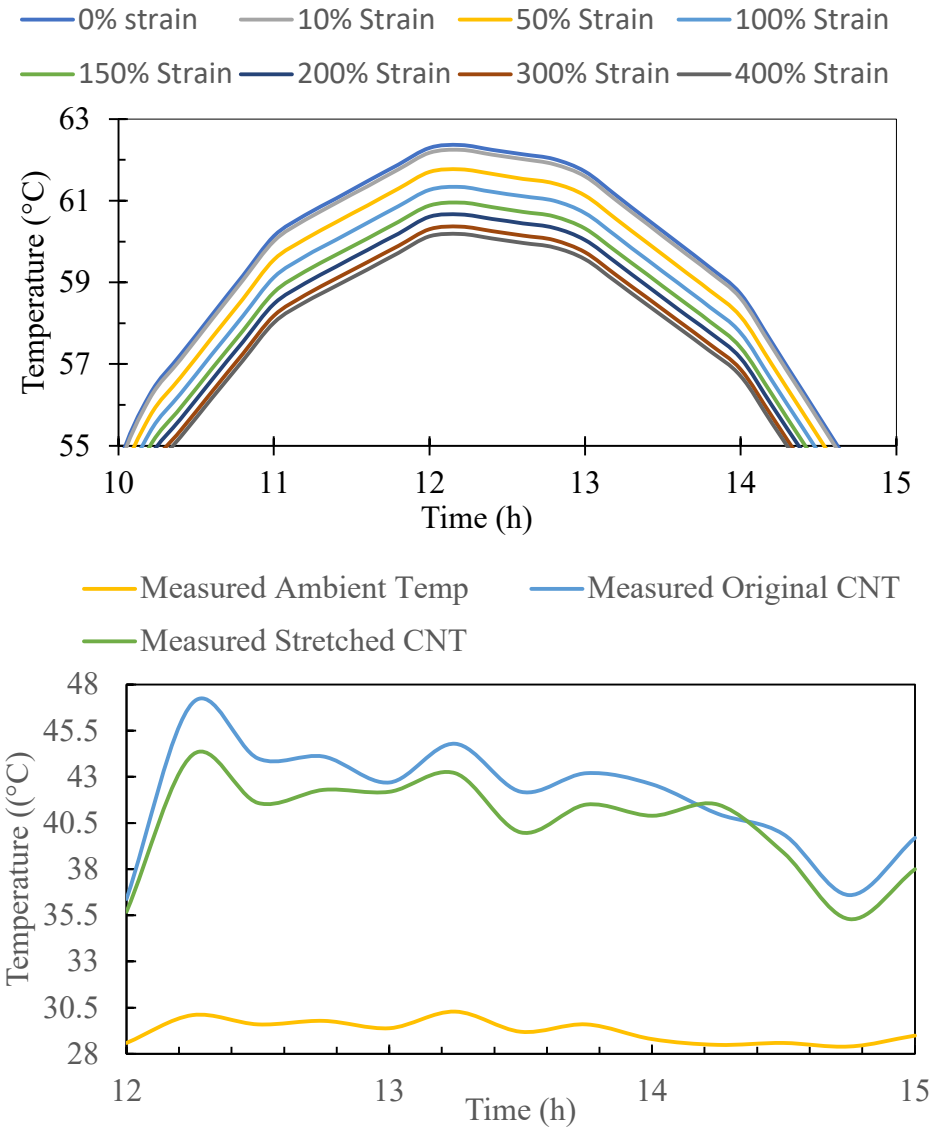

Figure 29: Simulated temperature (top) vs. experimental data (bottom)

It should be emphasized that the work shown here is for the purposes of demonstrating how the simulated temperature responses are similar to that of the measured i.e. how straining and further straining can result in a reduction in temperature. In both cases a similar temperature diffidence is observed; a maximum temperature difference of 2.45 ℃ and 2.8 ℃ was observed in the simulated (400% strain vs no strain) and experimental case (80% strain vs no strain) respectively.

Chapter 4: Conclusions and Future work

4.1 Conclusions

Based on the experimental characterization a 3D model was developed to represent the complex structure seen in CNT films. The developed model was simulated using raytracing: a geometrical optics method conventionally reserved for models with a very large size parameter. However, under sufficient justification an unconventional method was used to obtain reliable results. The simulation results obtained from the 3D model at different levels of strain were used to develop a hypothesis. The hypothesis viewed the surface of the CNT film to be composed many pits. As the film was strained, these pits were visualized to become shallower and broader as previously explained by figure 23; allowing for more light rays to escape from the bottom of the pit. Note the mechanism behind the developed hypothesis is not uniquely limited to CNT films. Hence, the mechanism behind enhanced reflectivity with increasing strain can be broadly applied to any material synthesized to exhibit a fibrous sponge structure similar to those of CNT. However, due to the difference in the intrinsic reflectivity of different materials, the degree of strain-dependent reflectivity enhancement will vary. For example, a fibrous sponge of silver will have significantly more second-order reflections than those of CNT giving a better reflectivity enhancement on straining. Finally, it can be concluded that the work presented in this thesis can be used by future researchers in the design of enhanced strain-dependent photonic structures for improved thermoregulation.

4.2 Limitations

The work presented in this thesis was performed under certain limitations and assumptions. All assumptions were made with sufficient justifications. However, it is important to educate the reader on the assumptions used to overcome the limitations that had been present during the development of this thesis.

Due to the complex morphology of the CNT film, the only feasible simulation scheme available to the author was raytracing, this scheme was used in a domain traditionally reserved for rigorous solvers such as FDTD or RCWA. However, a sufficient justification was provided in section 3.7. Additionally, due to the lack refractive indexes in the desired spectral range the material assignment to CNT was graphite; the closest available material to CNT. For the temperature simulations in Chapter 4 the simulated results of figure 19 was extended till 2.5 μm. Once extended beyond 1.5 μm, the raytracing model becomes not applicable [28]. This was done to calculate the absorptivity in the entire solar region. Finally, the work in this thesis was limited to the measurement of 3 CNT samples with the comparison between 80% strain and no strain. If more measurements of different levels of strains were available, the hypothesized trend could be experimentally verified.

4.3 Future Work

The increase in strain-dependent reflectivity of the simple model developed for the comparison between raytracing and RCWA in section 3.6 was found to be better than the original simulated CNT model. The simpler model exhibited a change of 0.145 in reflectivity between the 400% strain case and zero strain case, whereas the original model developed to mimic the CNT changed 0.047 between similar strains. Thus, is it clear that specifically ordered arrangement of materials can exhibit a stronger strain-dependent changed in reflectivity. Using this understanding the dimensions of the simple model, such as the cubes spacing in X, Y and Z directions and the number of layers of cubes in the positive Z direction were further changed for better reflectivity enhancement. Additionally, the substrate of the simpler model was substituted for a more reflective silver coating. Figure 30 shows the variation of optical properties vs. strain for the new silver backed ordered design.

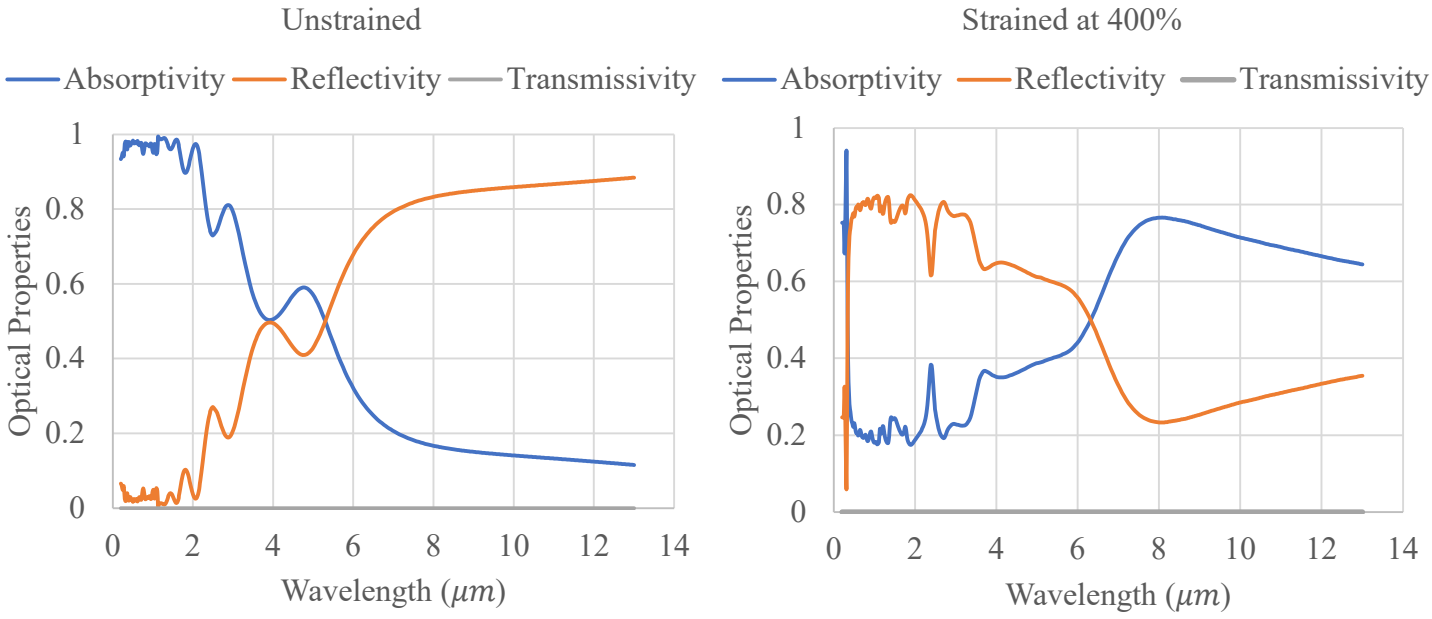

Figure 30: Optical properties of the silver backed design

Using these emissivity values, the simulated temperature variation is shown in figure 31. Comparing with figure 3 in the introduction section it is clear that the unstrained case behaves close to an ideal solar heater and the strained case has the preferred attributes that of an ideal passive cooler.

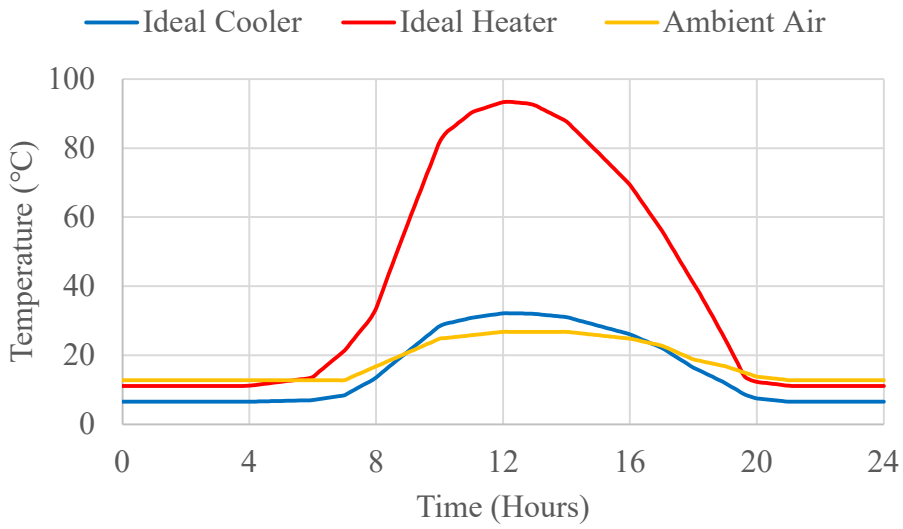

Figure 31: Temporal temperature variation of optimized design

The improved silver back design shows a large temperature modulation range of 61℃ at the maximum temperature point at noon, additionally the unstrained case exhibits cooling properties at times departing away from noon.

In terms of continuing future work from the current understanding, the existing design can be further improved by the use of composite textured surfaces for the improved mid-IR emissivity allowing for improved cooling. Furthermore, a passive actuation mechanism for CNT film can be implemented via the use of temperature dependent SMA springs [21], the proper integration of SMA springs with CNT films will pave the way for the creation of a smart material capable of self-thermal regulation.

References

[1] Rytov, S. M. (1959). Theory of electric fluctuations and thermal radiation (No. AFCRC-TR-59-162). AIR FORCE CAMBRIDGE RESEARCH LABS HANSCOM AFB MA.

[2] Howell, J. R., Menguc, M. P., & Siegel, R. (2010). Thermal radiation heat transfer. CRC press.

[3] Athanasopoulos, N., & Siakavellas, N. J. (2015). Programmable thermal emissivity structures based on bioinspired self-shape materials. Scientific reports, 5(1), 1-13.

[4] Victoria, M., Domínguez, C., Askins, S., Antón, I., & Sala, G. (2012). ASTM G173 standard tables for reference solar spectral irradiances. Japanese Journal of Applied Physics, AM15D, 10ND06. http://doi.org/10.1143/JJAP.51.10ND06

[5] Lord, S. D. (1992). Technical Memorandum 103957. Tech. rep., NASA.

[6] Raman, A. P., Abou Anoma, M., Zhu, L., Rephaeli, E., & Fan, S. (2014). Passive radiative cooling below ambient air temperature under direct sunlight. Nature, 515(7528), 540-544.

[7] Zhai, Y., Ma, Y., David, S. N., Zhao, D., Lou, R., Tan, G., ... & Yin, X. (2017). Scalable-manufactured randomized glass-polymer hybrid metamaterial for daytime radiative cooling. Science, 355(6329), 1062-1066.

[8] Nie, X., Yoo, Y., Hewakuruppu, H., Sullivan, J., Krishna, A., & Lee, J. (2020). Cool White polymer coatings based on Glass Bubbles for Buildings. Scientific reports, 10(1), 1-10.

[9] Dyachenko, P. N., Molesky, S., Petrov, A. Y., Störmer, M., Krekeler, T., Lang, S., ... & Eich, M. (2016). Controlling thermal emission with refractory epsilon-near-zero metamaterials via topological transitions. Nature communications, 7(1), 1-8.

[10] Cui, Y., Fung, K. H., Xu, J., Ma, H., Jin, Y., He, S., & Fang, N. X. (2012). Ultrabroadband light absorption by a sawtooth anisotropic metamaterial slab. Nano letters, 12(3), 1443-1447.

[11] Wu, D., Liu, C., Liu, Y., Xu, Z., Yu, Z., Yu, L., ... & Ye, H. (2018). Numerical study of a wide-angle polarization-independent ultra-broadband efficient selective metamaterial absorber for near-ideal solar thermal energy conversion. RSC advances, 8(38), 21054-21064.

[12] Jiang, Y. (2014). An outlook review: Mechanochromic materials and their potential for biological and healthcare applications. Materials Science and Engineering: C, 45, 682-689. doi:10.1016/j.msec.2014.08.027

[13] Beyer, M. K., & Clausen-Schaumann, H. (2005). Mechanochemistry: The Mechanical Activation of Covalent Bonds. Chemical Reviews, 105(8), 2921-2948. doi:10.1021/cr030697h

[14] Carraway, E. R., Demas, J. N., Degraff, B. A., & Bacon, J. R. (1991). Photophysics and photochemistry of oxygen sensors based on luminescent transition-metal complexes. Analytical Chemistry, 63(4), 337-342. doi:10.1021/ac00004a007

[15] Hays, D. S., Prince, R. B., & Bommarito, G. M. (2011). U.S. Patent No. 8,063,164. Washington, DC: U.S. Patent and Trademark Office.

[16] Peterson, G. I., Larsen, M. B., Ganter, M. A., Storti, D. W., & Boydston, A. J. (2015). 3D-printed mechanochromic materials. ACS applied materials & interfaces, 7(1), 577-583.

[17] Chan, E. P., Walish, J. J., Urbas, A. M., & Thomas, E. L. (2013). Mechanochromic photonic gels. Advanced Materials, 25(29), 3934-3947.

[18] Juhl, S. B., Chan, E. P., Ha, Y. H., Maldovan, M., Brunton, J., Ward, V., ... & Vaia, R. A. (2006). Assembly of Wiseana iridovirus: viruses for colloidal photonic crystals. Advanced Functional Materials, 16(8), 1086-1094.

[19] Sala-Casanovas, M., Krishna, A., Yu, Z., & Lee, J. (2019). Bio-inspired stretchable selective emitters based on corrugated nickel for personal thermal management. Nanoscale and Microscale Thermophysical Engineering, 23(3), 173-187.

[20] Krishna, A., Kim, J. M., Leem, J., Wang, M. C., Nam, S., & Lee, J. (2019). Ultraviolet to mid-infrared emissivity control by mechanically reconfigurable graphene. Nano letters, 19(8), 5086-5092.

[21] Liang, G., Sadeghifard, A., Krishna, A., Lee, J., & Peraza Hernandez, E. A. (2019, October). Modeling and analysis of a shape memory alloy-based adaptive regulator for thermal management. In International Electronic Packaging Technical Conference and Exhibition (Vol. 59322, p. V001T07A002). American Society of Mechanical Engineers.

[22] Yang, G., Choi, W., Pu, X., & Yu, C. (2015). Scalable synthesis of bi-functional high-performance carbon nanotube sponge catalysts and electrodes with optimum C–N–Fe coordination for oxygen reduction reaction. Energy & Environmental Science, 8(6), 1799-1807.

[23] Choi, W., Choi, K., & Yu, C. (2018). Ultrafast nanoscale polymer coating on porous 3D structures using microwave irradiation. Advanced Functional Materials, 28(4), 1704877.

[24] Utel, F., Cortese, L., Wiersma, D. S., & Pattelli, L. (2019). Optimized White Reflectance in Photonic-Network Structures. Advanced Optical Materials, 7(18), 1900043.

[25] Freniere, E. R., Gregory, G. G., & Hassler, R. A. (1999, September). Edge diffraction in Monte Carlo ray tracing. In Optical design and analysis software (Vol. 3780, pp. 151-157). International Society for Optics and Photonics.

[26] Leow, S. W., Corrado, C., Osborn, M., & Carter, S. A. (2013, September). Monte Carlo ray-tracing simulations of luminescent solar concentrators for building integrated photovoltaics. In High and Low Concentrator Systems for Solar Electric Applications VIII (Vol. 8821, p. 882103). International Society for Optics and Photonics.

[27] Byun, S. J., Byun, S. Y., Lee, J., Kim, J. W., Lee, T. S., Kim, W. M., ... & Cho, K. (2011). An optical simulation algorithm based on ray tracing technique for light absorption in thin film solar cells. Solar energy materials and solar cells, 95(1), 408-411.

[28] Tomboulian, B. N., & Hyers, R. W. (2017). Predicting the effective emissivity of an array of aligned carbon fibers using the reverse monte carlo ray-tracing method. Journal of Heat Transfer, 139(1).

[29] Djurišić, A. B., & Li, E. H. (1999). Optical properties of graphite. Journal of applied physics, 85(10), 7404-7410.

[30] Wang, Y., Cho, S., Thiedmann, R., Schmidt, V., Lehnert, W., & Feng, X. (2010). Stochastic modeling and direct simulation of the diffusion media for polymer electrolyte fuel cells. International journal of heat and mass transfer, 53(5-6), 1128-1138.

[31] Thomson, K. T., & Gubbins, K. E. (2000). Modeling structural morphology of microporous carbons by reverse Monte Carlo. Langmuir, 16(13), 5761-5773.

[32] Glassner, A. S. (1989). Surface physics for ray tracing. An introduction to ray tracing, 121-160.

[33] Yang, P., Ding, J., Panetta, R. L., Liou, K. N., Kattawar, G. W., & Mishchenko, M. (2019). On the convergence of numerical computations for both exact and approximate solutions for electromagnetic scattering by nonspherical dielectric particles. Electromagnetic waves (Cambridge, Mass.), 164, 27.